ACS APPLIED MATERIALS & INTERFACES

Research Article

www.acsami.org

Evaluating Pristine and Modified SnS_2 as a Lithium-Ion Battery Anode: A First-Principles Study

Zhixiao Liu,[†] Huiqiu Deng,*[,‡] and Partha P. Mukherjee*[,†]

[†]Department of Mechanical Engineering, Texas A&M University, College Station, Texas 77843, United States

[‡]Department of Applied Physics, School of Physics and Electronics, Hunan University, Changsha 410082, China

ABSTRACT: Li intercalation and diffusion in pristine and modified SnS_2 interlayer are studied by a first-principles approach. The results predict that the octahedral interstitial site is energetically favored for Li intercalation. The minimum energy path of Li diffusion in SnS_2 interlayer is investigated by climbing image nudged elastic band method. It is found that Li atom diffuses from one energetically favored octahedral interstitial site to the neighbor one via tetrahedral interstitial site. The expansion of interlayer spacing is beneficial for decreasing the diffusion barrier. Ce dopant negatively impacts the Li diffusivity although it can optimize the interlayer spacing. Geometric structures of Li_xSnS_2 ($0 < x \leq 3$) are investigated to understand the lithiation-induced volume expansion and atomic structure change. The lithiation process can be divided into two stages. When Li content (x in Li_xSnS_2) is less than 1, the volume expansion is not dramatic and only S atoms capture electrons from Li atoms. When Li content is larger than 1, Sn^{4+} cations are significantly reduced, S−Sn−S trilayer gradually decomposes, and Li_xS_2 ($1 \leq x \leq 3$) layer forms between two Sn monolayers. The mechanism of volume expansion is elucidated in this study.

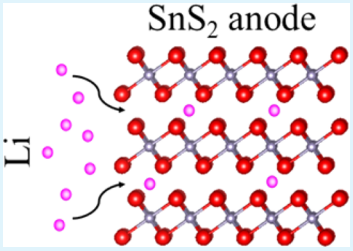

KEYWORDS: *tin disulfide anode, two-dimensional nanostructure, interlayer diffusion, volume expansion, first-principles calculation*

INTRODUCTION

Great attention has been attracted to improving lithium-ion batteries (LIBs) to meet the requirements for electric vehicles (EVs) application.[1−4] A large quantity of novel materials has been synthesized for LIB cathode to achieve this goal.[5−9] Additionally the LIB performance can also be significantly improved by employing a favorable processing scheme.[10−16] In the aspect of anode material, conventional carbon-based anode is a limitation due to the low theoretical specific capacity, 372 mAh/g, according to LiC_6. To avoid this problem, research on LIB anode focuses on developing new materials that have high specific capacity, stable cycling behavior, and economical synthetic method to replace the carbon-based materials.[17−20]

Tin (Sn), which is abundant and cheap, is an interesting and competitive candidate as LIB anode material because of its high theoretical specific capacity, 994 mAh/g, according to $Li_{4.4}Sn$.[21] However, Sn anode has not been commercialized because the volume change during the lithiation/delithiation cycling destroys anode structure. Several schemes have been developed to synthesis innovative Sn nanostructures to tolerate the volume variation and capacity fading.[22−25] Nowadays, synthesis novel nanostructured materials is an effective way to improve the performance of energy storage devices.[26−28] Sn-based materials with layered crystalline, especially tin disulfide (SnS_2), attract a lot of interest as lithium storage materials because the layered structure can minimize the volume change during lithiation/delithiation cycling[29] and improve the Li mobility.[30] Lefebvre-Devos et al. investigated Li insertion in SnS_2 and found that the interlayer spacing did not increase when the atom ratio of Li to Sn was below 1.22.[31] Kim et al. synthesized crystalline SnS_2 nanosheets with a one-step solvothermal process.[32] Electrochemical cycling tests showed that the thinner nanosheets were more beneficial for reaction kinetics and capacity retention. Using a facile hydrothermal method, Wang et al. synthesized two-dimensional SnS_2 nanoplates.[33] It was found that the size and crystallinity of the SnS_2 nanoplates determined the electrochemical performance of the anode. Zhai et al. coated SnS_2 nanosheets on multiwall carbon nanotubes (MWCNTs) and found the composite had better lithium storage performance than bare SnS_2 nanosheets.[34] Graphene is another support material for SnS_2 nanosheets. SnS_2 nanosheets with a thickness of 2−5 nm were anchored on graphene with (001) direction by a facile one-step solvothermal method.[35] SnS_2 nanosheet/graphene composite significantly enhanced cycling stability and rate capacity because the composite buffered the volume changes. SnS_2 nanosheet/graphene composite could also improve sodium storage performance and cycling stability as sodium ion battery (SIB) anode.[36] Zhong et al. synthesized a new layered SnS_2 nanosheet thinner than five atomic layers.[37] In their experiment, SnS_2 nanosheets were vertically anchored on Sn foil, and the interlayer spacing was increased by 0.2 Å compared to the parallel anchored SnS_2. Substituting Sn with cerium (Ce) was an effective method to increase the interlayer spacing.[38,39] The optimized interlayer spacing provided large space for lithium intercalation and deintercalation, which could improve the LIB cycling stability.

Although experiments have proved that Ce substitution of Sn in SnS_2 is an effective way to improve the anode performance,

Received: October 6, 2014
Accepted: January 28, 2015
Published: January 28, 2015

DOI: 10.1021/am5068707
ACS Appl. Mater. Interfaces 2015, 7, 4000−4009

the interaction mechanism between Li and SnS_2 matrix is not yet well understood. It was claimed that the Ce dopant can modify the local electronic structure which affects the Li diffusion behavior.[38,40] However, there has been no theoretical study to justify the mechanisms of Li−Ce−SnS_2 interaction from the aspect of electronic structure analysis. Additionally, the volume expansion and crystal distorition during the lithiation determine the stability of SnS_2 anode. In this study, we plan to use a first-principles approach to investigate the behavior of Li intercalation and diffusion in SnS_2 crystal and elucidate the Li−SnS_2 interaction based on electronic structure analysis. The volume expansion and the crystal structure variation induced by Li intercalation will also be studied. Finally, the efficacy of Ce dopant in SnS_2 will be evaluated.

COMPUTATIONAL METHODS

First-principles approach has been widely used to design energy storage devices and understand Li insertion and diffusion in electrode materials.[41−43] However, there is no theoretical study for fundamentally understanding the behaviors of interstitial Li in pristine and modified SnS_2 interlayer. In the present study, a first-principles approach was performed to study the Li insertion and diffusion in SnS_2, and the effect of Ce dopant on Li diffusivity was also evaluated.

All calculations in the present work were implemented in Vienna ab inito simulation package (VASP),[44,45] which was a first-principles calculator based on the density functional theory (DFT).[46] The electron−ion interaction was described by the projector augmented wave (PAW) method,[47] and the electron−electron exchange correlation was described by the generalized gradient approximation (GGA) of Perdew−Burke−Ernzerhof (PBE) functional.[48] The cutoff energy for the plane wave basis is set to 300 eV. All calculations are based on 3 × 3 × 2 supercell (18 Sn atoms and 36 S atoms) with a 3 × 3 × 3 k-points mesh which was generalized by Monkhorst−Pack (MP) technique.[49] The force convergence criterion for optimizing atom position was set up to 0.02 eV/Å. The Ce-doped SnS_2 was modeled by one Ce atom replacing one Sn atom in the 3 × 3 × 2 supercell. The dopant concentration in this study approaches 5 mol %, which related to better reversible capacity and cycle stability than SnS_2 compounds with other concentrations.[38]

The energetically favored site for interstitial Li is searched by comparing the formation energy (E_f), which is calculated as

$$E_f = E_{Li@sc} - E_{sc} - E_{Li}$$

Here $E_{Li@sc}$ is the total energy of interstitial Li in the SnS_2 supercell, E_{sc} is the total energy of the supercell, and E_{Li} is the energy per Li atom in the perfect Li crystal. A negative E_f represents an exothermic reaction, and a more negative value indicates a more energetically stable configuration. The minimum energy path (MEP) for Li diffusion from one interstitial site to its neighbor one was searched by climbing image nudged elastic band (CI-NEB).[50] To search the MEP, five images were linearly generated between initial state and final state. The diffusion barrier was defined as the energy difference between the saddle image and the initial state.

RESULTS AND DISCUSSIONS

SnS_2 has a hexagonal crystal structure with the space group $P\bar{3}m1$.[51] The lattice parameters from the present GGA-PBE calculation are a = 3.67 Å and c = 6.12 Å, as shown in Table 1, which agree well with previous GGA-PW91 results (a = 3.69 Å and c = 6.19 Å)[52] and ab initio molecular dynamics (AIMD) results (a = 3.66 Å and c = 6.06 Å).[53] These theoretical results are a bit larger than the experimental ones. This deviation is typical for the DFT-GGA approach.[52] The bond length between Sn and S (D_{Sn-S}) is 2.58 Å, and it agrees well with the bond length calculated by GGA-PW91 approach.[52]

Table 1. Geometric Parameters of SnS_2 Crystal[a]

	a (Å)	c (Å)	D_{Sn-S} (Å)
pristine SnS_2.	3.67	6.12	2.58
Ce-doped SnS_2	3.72	6.20	2.60
expanded $SnSn_2$	3.72	6.20	2.61
experiment[51]	3.65	5.90	2.55
GGA-PW91[52]	3.69	6.19	2.59
AIMD[53]	3.66	6.06	–

[a] a and c denote lattice parameters, and D_{Sn-S} denotes the length of Sn−S bond.

In a pristine SnS_2 3 × 3 × 2 supercell, there are two kinds of interstitial sites. An octahedral interstitial site (OIS) is the center of octahedron composed of six S atoms, and a tetrahedral interstitial site (TIS) is the center of tetrahedron composed of four S atoms (Figure 1a). In the present work, we also considered the properties of interstitial Li in a Ce-doped 3 × 3 × 2 SnS_2 supercell. The doped SnS_2 is modeled by substituting a Sn atom with a Ce atom, which means that the mole fraction of dopant approaches 5 mol %. The optimized lattice parameters of Ce-doped are a = 3.72 Å, c = 6.20 Å. Compared with the pristine SnS_2, the dopant expands the interlayer distance between two SnS_2 single sheets by 1.26%. Experimentally, 5 mol % Ce dopant can increase the interlayer distance by 1.05%.[38] Our simulations also demonstrate that the Sn−S bond length (D_{Sn-S}) is elongated to 2.60 Å. The bond length between Ce and S atoms is 2.73 Å, which is 0.13 Å longer than the Sn−S bond. To deeply understand the effects of Ce dopant and the accompanying volume expansion, we also consider a nondoped SnS_2 with lattice parameters equaling those of Ce-doped SnS_2. In the expanded SnS_2, the Sn−S bond length is 2.61 Å, slightly longer than that in Ce-doped SnS_2.

Table 2 shows the formation energy of Li atom at different interstitial sites. For pristine SnS_2, the formation energy of Li atom occupying OIS is −1.72 eV, and the averaged Li−S bond length ($\bar{D}_{Li-S}$) is 2.62 Å. The formation energy of Li atom occupying TIS is −1.4.9 eV, which is 0.22 eV higher than that of Li occupying OIS. The $\bar{D}_{Li-S}$ of Li occupying TIS is 2.37 Å. It is obvious that OIS is energetically favored for Li occupation. Experimentally, Li insertion mechanism was systematically investigated by ^{119}Sn Mössbauer and XANES spectra,[31] and results showed that interstitial Li occupied the octahedral site without distorting SnS_2 crystal structure. Bader charge analysis[54−56] shows that Li is positively charged by 1 e, while S atoms are negatively charged by around 2 e. Hence there is an attractive Coulomb force between interstitial Li and a coordination S, which makes a contribution to generate negative formation energy. The $\bar{D}_{Li-S}$ of Li occupying TIS is shorter than that of Li occupying OIS; thereby, the attractive force between the interstitial Li and one coordination S is stronger. However, Li atom at OIS can interact with two more S atoms than Li at TIS. Consequently, the formation energy of Li occupying OIS is more negative, and this site is more energetically favored.

For Ce-doped SnS_2, two OISs are considered (Figure 1b): one is directly above the Ce substitution (OIS_1), and the other one is above the Sn atom which is the first nearest neighbor of the Ce substitution (OIS_2). For TIS, only the one near the Ce atom is considered in the present study. According to Table 2, the OISs are energetically favored for accepting interstitial Li. The E_f values for OIS_1 and OIS_2 are −1.87 and 1.85 eV, respectively, which are 0.15 eV lower than the Li at OIS of

DOI: 10.1021/am5068707
ACS Appl. Mater. Interfaces 2015, 7, 4000−4009

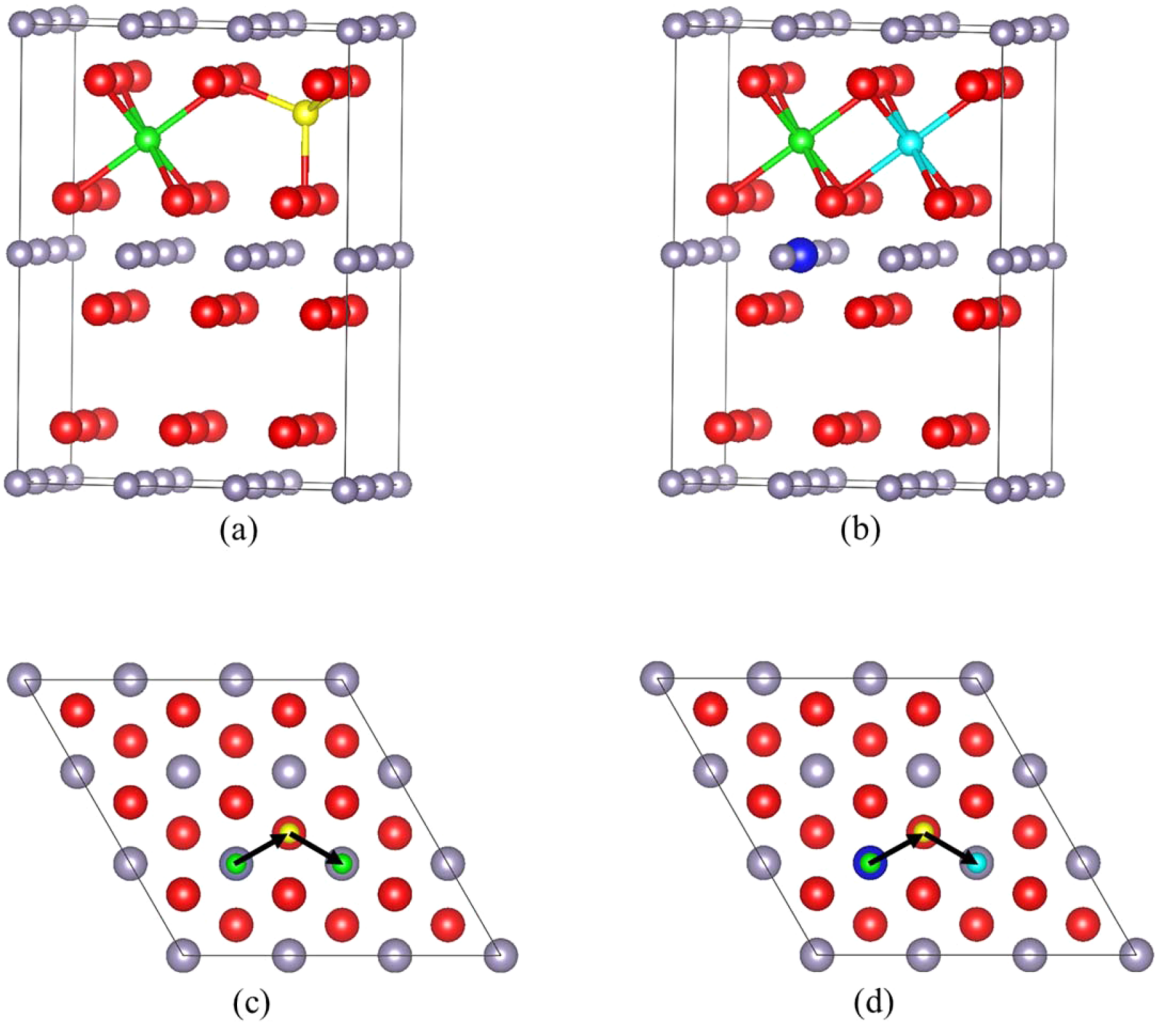

Figure 1. Schematic illustration of 3 × 3 × 2 (a) nondoped SnS_2 with OIS (green ball) and TIS (yellow ball), and (b) Ce-doped SnS_2 with OIS_1 (green ball) and OIS_2 (light blue ball). The Ce dopant is represented by a dark blue ball. Sn atoms and S atoms are represented by gray balls and red balls, respectively. Part (c) illustrates the Li diffusion from one OIS to another one via a TIS, and (d) illustrates the Li diffusion from OIS_1 to OIS_2 via a TIS. Both diffusion trajectories are projected to the (001) plane which is vertical to the *c* axis.

Table 2. Energetic and Geometric Parameters of Interstitial Li in the SnS_2 Crystal[a]

	pristine SnS_2		Ce-doped SnS_2			expanded SnS_2	
	OIS	TIS	OIS_1	OIS_2	TIS	OIS	TIS
E_f	−1.72	−1.49	−1.87	−1.85	−1.65	−1.81	−1.65
$\bar{D}_{Li-S}$	2.62	2.37	2.68	2.65	2.40	2.66	2.40

[a] E_f denotes the formation energy (in eV), and $\bar{D}_{Li-S}$ is the averaged bond length (in Å) between Li and its coordinating S atoms.

pristine SnS_2. For Li at TIS, the E_f is lowered by 0.20 eV. The averaged Li−S bond lengths are increased by 0.03 to 0.06 Å in the Ce-doped SnS_2 due to its larger lattice parameters than those of the pristine SnS_2.

To further understand the effects of Ce dopant and volume expansion on the formation energy of the interstitial Li atom, a nondoped SnS_2 supercell with lattice parameters equaling to Ce-doped ones is investigated (Table 2). It is found that the E_f of TIS in the expanded SnS_2 is −1.65 eV, which is equal to E_f of TIS in the Ce-doped supercell. Oppositely, for Li at OIS, the E_f of expanded SnS_2 is −1.81 eV, which approaches the mean value of the formation energy in pristine SnS_2 and Ce-doped SnS_2. Based on the information from Table 2, it can be inferred that the volume expansion plays an important role in determining the E_f of Li atom at TIS. Conversely, Ce dominantly affects the E_f of Li atom at OIS.

The diffusion properties of interstitial Li in SnS_2 matrix were studied in the present study. The MEP for Li diffusion from an energetically favored OIS to the adjacent one was obtained by the CI-NEB method. Present calculations predict that interstitial Li tends to diffuse from one OIS to the neighbor one via a TIS (Figure 1c and d). The energy barrier along the diffusion path is shown in Figure 2. Five images are linearly inserted between OIS site and TIS site. In the diffusion barrier plot, each point represents the energy difference between that image and the initial state (OIS site). The diffusion barrier is the energy difference between the saddle point and the initial point (OIS site). The diffusion barrier from OIS to TIS is 0.38

DOI: 10.1021/am5068707
ACS Appl. Mater. Interfaces 2015, 7, 4000−4009

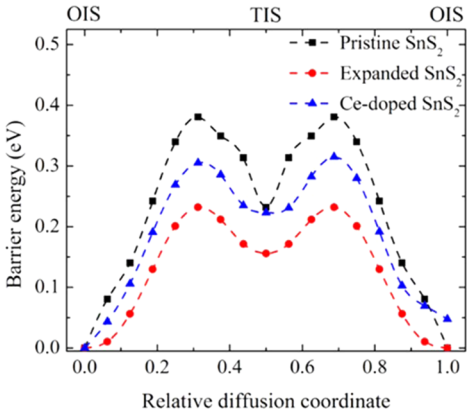

Figure 2. Barrier of Li diffusion in SnS_2.

eV in the pristine SnS_2 matrix, which is as high as the Li diffusion barrier in pure Sn bulk.[57] The volume expansion of nondoped SnS_2 can decrease the Li diffusion barrier to 0.23 eV, which is even lower than the diffusion barrier of Li in some bulk anode materials[57,58] and two-dimensional nanostructure such as bilayer graphene,[59] silicene,[60] and MoS_2.[61] According to the Arrhenius equation, $D = D_0 \exp(-E_b/\kappa T)$, it can be estimated that the volume expansion can increase the Li diffusion coefficient (D) to 3 orders of magnitude to the pristine SnS_2 at room temperature because the volume expansion lowers the diffusion barrier (E_b). Similarly, the Li diffusion barrier from TIS to OIS in the expanded SnS_2 is 0.07 eV lower than that in the pristine SnS_2. Previous research on Li diffusion in bulk MoS_2 and bilayer MoS_2 reported that the bilayer structure improved the Li mobility due to larger interlayer spacing of the bilayer than the bulk.[61] Our results also prove that interlayer spacing expansion is beneficial for improving the Li mobility in the SnS_2 electrode. Experimentally, Ce substituting Sn is an effective way to make SnS_2 expand.[38,39] The present CI-NEB calculation predicts that the OIS_1-to-TIS diffusion barrier is 0.31 eV, which is lower than the pristine SnS_2 but higher than the nondoped expanded SnS_2. The result indicates that the Ce substitution counteracts the barrier reduction caused by the volume expansion. To this end, it is necessary to develop an approach to synthesis volume-expanded SnS_2 nanostructure without employing dopant which impedes Li diffusion. Recently, ultrathin SnS_2 nanosheet arrays vertically aligned on the Sn foil were synthesized by a simple biomolecule-assisted method.[37] It was found that the interlayer distance in the nanosheet is about 0.2 Å larger than that in the bulk, and the vertical nanosheet had higher averaged discharge capacity than the theoretical value.

It should be noted that the diffusion coefficient (D) in the realistic condition is not only determined by the single Li atom diffusion barrier (E_b). In a LIB electrode, the electronic conductivity and defects in the diffusion path play important roles in determining the Li diffusivity.[62] In addition, the local Li concentration and net charge of the system also affect the diffusion barrier.[57,60,63,64] However, single atom diffusion is reasonable enough to qualitatively understand the Li diffusion mechanism in the SnS_2 interlayer.

Electronic structures of interstitial Li and its surrounding atoms are analyzed to deeply understand Li behaviors in the SnS_2 interlayer. The Bader charge analysis demonstrates that a single interstitial Li atom loses its valence electron in the SnS_2 matrix. The transferred negative charge is captured by S atoms. It is found that S atoms coordinating with interstitial Li atom obtain more charge than the others. Figure 3 shows the total

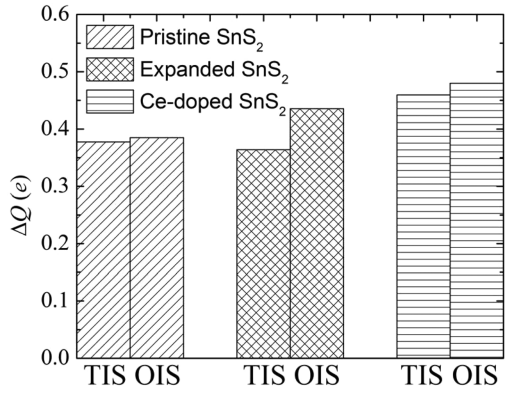

Figure 3. Charge increase (ΔQ) of S atoms coordinating with interstitial Li atoms in pristine, expanded, and Ce-doped SnS_2 matrices.

charge transferred from interstitial Li atom to coordinating S atoms (ΔQ). For pristine SnS_2, coordinating S atoms get 0.378 *e* negative charge from TIS Li and 0.385 *e* negative charge from OIS Li. Similarly, coordinating S atoms get more negative charge from OIS Li than from TIS Li for Ce-doped or expanded SnS_2. Additionally, coordinating S atoms in Ce-doped SnS_2 obtain more negative charge than those in the other two SnS_2 matrices. The amount of the charge transfer coincides with the interstitial Li formation energy E_f. It is clear that a larger charge transfer to coordinating S atoms corresponds to a more negative formation energy. The formation energy difference between OIS and TIS in pristine SnS_2 is the same as that in Ce-doped SnS_2 as shown in Table 2 and Figure 2. Similarly, as shown in Figure 3, the ΔQ difference between TIS and OIS in pristine SnS_2 agrees well with the ΔQ in Ce-doped SnS_2.

Interstitial Li-induced charge redistribution is shown in Figure 4. Although Bader charge analysis demonstrates that the interstitial Li loses its valence electron, Li−S bond is not an ideal ionic bond. The covalent component can be observed in Figure 4. As shown in Figure 4, there are charge aggregation regions between interstitial Li and coordinating S atoms. For Li at TIS, the S−Li−S bond angle and the shape of charge aggregation region correspond to the geometric parameters of tetrahedral. It is inferred that the valence component between Li and S atoms is dominated by sp^2 hybridization. The interstitial Li also generates electron redistribution between coordinating S atom layers and their adjacent Sn atom layers. As shown in Figure 4, electron depletion regions appear between S layer and Sn layer, which means the Li foreigner weakens the interaction between S layer and Sn layer. The interaction between S and Sn layers is weaker in SnS_2 with TIS Li than in SnS_2 with OIS Li. It is obvious that the volume of electron depletion region is larger with TIS Li. As shown in the figures of difference charge density, the interstitial Li hardly affects electron distribution around Sn atoms, which means that there is no direct interaction between Li and Sn. However, for Ce-doped SnS_2, although Li foreigner does not interact with Sn atoms, the foreigner can induce an electron redistribution around Ce atom as shown in Figure 4e and f. The Bader charge analysis shows that the Ce atom in the nonlithiated SnS_2 is positively charged by 1.863 *e*. The TIS Li and OIS_1 Li can make

DOI: 10.1021/am5068707
ACS Appl. Mater. Interfaces 2015, 7, 4000−4009

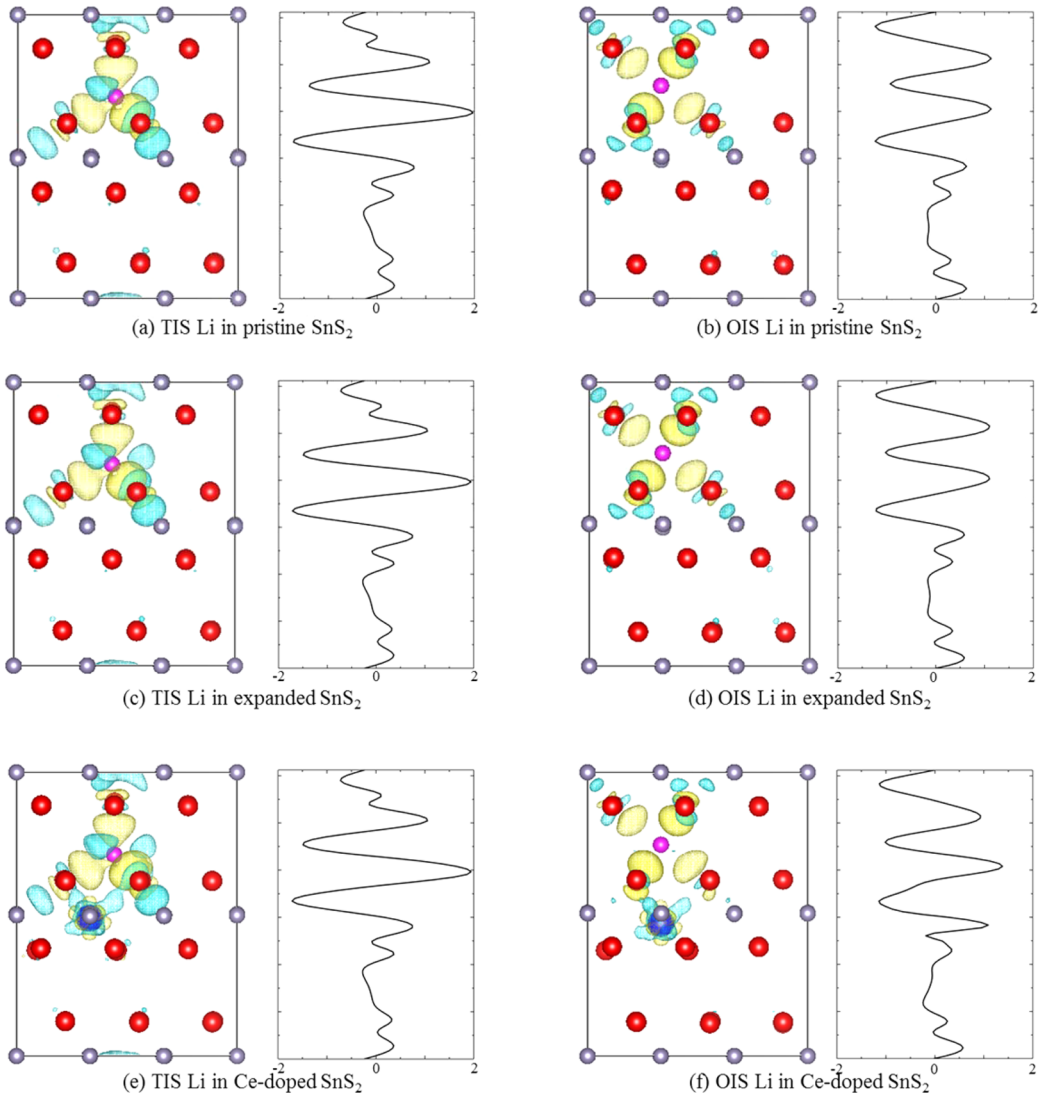

Figure 4. Difference charge density of interstitial Li in different SnS_2 matrix. The yellow isosurface (0.0012 e/Å^3) represents charge aggregation, and the light blue isosurface (0.0012 e/ Å^3) represents charge depletion. Plots accompanying different charge density figures demonstrate planar charge distribution along the [001] direction (c-axis).

the Ce positively charged by 1. 845 e and 1.808 e, respectively. It can be inferred that the Ce dopant is reduced by Li foreigner and there is a chemical interaction between Li atom and Ce atom.

The projected density of state (PDOS) of Li and a coordinating S atom is plotted in Figure 5 to understand the covalent interaction. It is can be seen that electrons are transferred to Li 2p orbitals which are empty at ground state. For both TIS Li and OIS Li, Li 2s and 2p states slightly overlap with S 3s states where the energy levels are around −12.5 eV below the Fermi level, which indicates a rather weak interaction between Li 2s as well as 2p states and S 3s states. The Li 2s and 2p states distributing around −5 to −1 eV hybridize with S 3p states more strongly than those hybridizing with S 2s states. This Li 2s and 2p/S 3p hybridization dominates the covalent interaction between interstitial Li and surrounding S atoms. The PDOS clearly shows that antibonding states above Fermi level are also dominated by hybridized Li 2s and 2p states and S 3p states. It is interesting that the volume expansion of nondoped SnS_2 subtly reduces the intensity of Li 2p states (antibonding states) around 3 eV above the Fermi level. This small reduction can explain the decrease of the interstitial formation energy. For Ce-doped SnS_2, the amount of antibonding states above Fermi level is significantly reduced, while the amount of bonding states increases obviously. In the same SnS_2 matrix, it is found that the OIS Li has less antibonding states than TIS Li, which indicates that the more negative formation energy of OIS Li can also be attributed to the stronger covalent interaction between Li and coordinating S atoms. Difference charge density demonstrates that interaction between interstitial Li and Ce can generate electron redistribution around Ce. Figure 6 shows the PDOS of interstitial Li and Ce. It can be seen that Li 2s and 2p states hybridize with Ce 5d and 4f states.

Volume expansion and crystal structure transition induced by lithiation potentially pose risks to the anode stability. Sn and SnO_2 based anode material always suffer from 200%∼300% volume expansion during the lithiation/delithiation process.[65] Si is another attractive anode material due to its high theoretical capacity and low discharge potential vs Li. However, the volume is quadrupled when the Si is fully lithiated to $Li_{4.4}Si$.[66,67] As a promising anode material, SnS_2 can buffer the lithiation-

DOI: 10.1021/am5068707
ACS Appl. Mater. Interfaces 2015, 7, 4000−4009

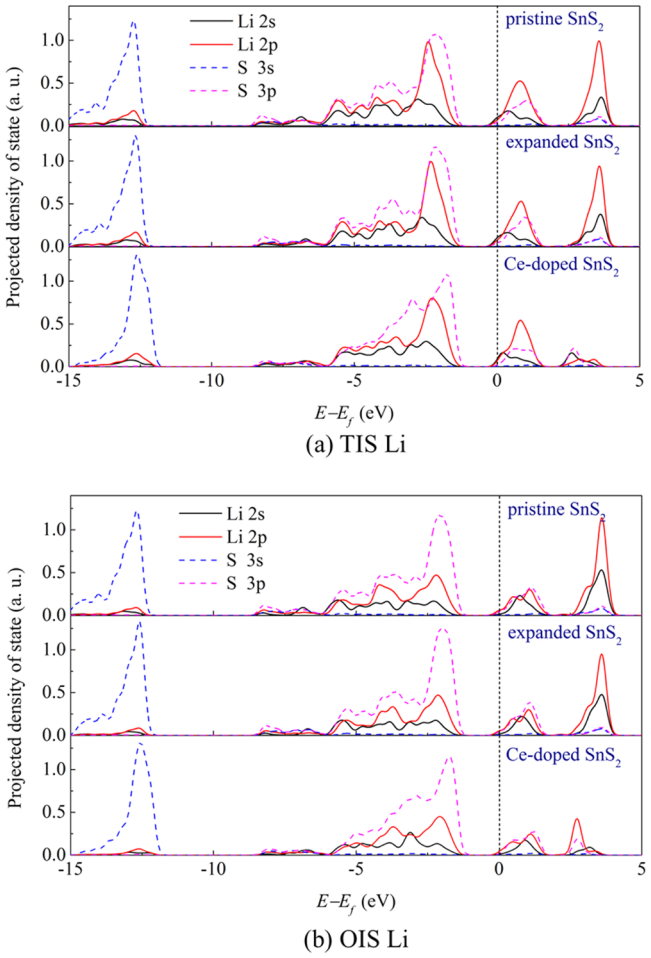

Figure 5. Projected density of states of Li at (a) TIS and (b) OIS in pristine, expanded, and Ce-doped SnS_2. Projected density of state is used to describe the interaction between the interstitial Li and a coordinating S atom. The intensity of Li states is multiplied by 10 to clearly show the hybridization. Black and red solid lines represent Li 2s and 2p states, respectively, and blue and violet dash lines represent S 3s and 3p states, respectively.

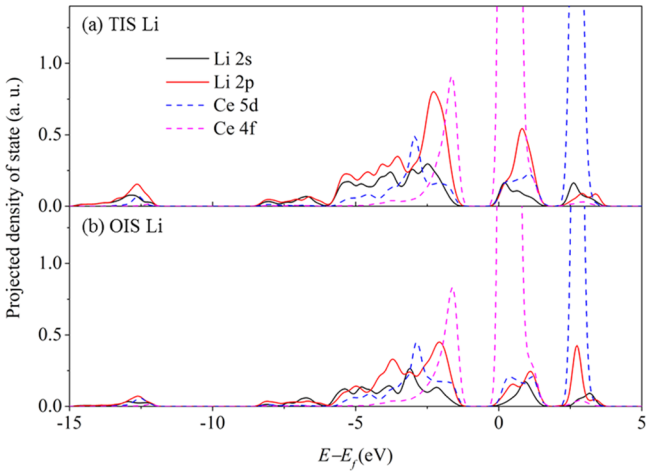

Figure 6. Projected density of states of Li at (a) TIS and (b) OIS in Ce-doped SnS_2. Projected density of state is used to describe the interaction between the interstitial Li and Ce atom. The intensity of Li states is multiplied by 10 to clearly show the hybridization. Black and red solid lines represent Li 2s and 2p states, respectively, and blue and violet dashed lines represent Ce 5d and 4f states, respectively.

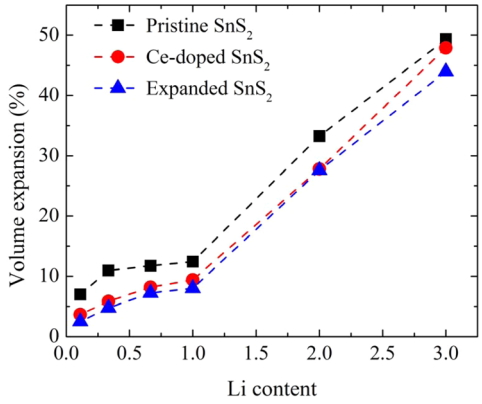

Figure 7. Volume expansion as the function of Li content.

induced volume expansion due to its layered nanostructure. However, there has been no literature reporting the volume expansion and crystal structure change due to Li intercalation. In the present study, we investigate the variation of the geometric properties of SnS_2 crystal during the lithiation process.

The volume expansion of Li_xSnS_2 $(0 \le x \le 3)$ is calculated in the present work. The lithiation induced volume expansion is calculated as

$$\alpha = \frac{V_{Li_xSnS_2} - V_{SnS_2}}{V_{SnS_2}} \times 100\%$$

Figure 7 shows the volume expansion of pristine, Ce-doped, and expanded SnS_2. It is found that the volume expansion increases slowly when the Li content is smaller than 1. The volume expansion of pristine SnS_2 is 11.74% at $x = 1$. The volume expansion at $x = 1$ is decreased to 8.19% and 7.22% in the Ce-doped and expanded SnS_2, respectively. Enyashin et al. studied Li intercalation in MoS_2, and found that the volume expansion is about 15%−20% at $x = 1$.[68] Hence, SnS_2 has greater advantage to tolerate the volume expansion induced by lithiation. For SnS_2-based anode, the volume expansion increases steeply when $x > 1$. Even so, the volume expansion of SnS_2-based anode is still lower than other anode materials. As shown in Figure 7, the volume expansion of SnS_2-based anode is less than 50% when the material is lithiated to Li_3SnS_2. For Mg anode and Sb anode, the volume expansions are 100% and 200% when they are lithiated to Li_3Mg and Li_3Sb, respectively. Additionally, Figure 7 also demonstrates that the lithiation-induced volume expansion of Ce-doped SnS_2 is less than that of pristine SnS_2 at the same Li content, and the expanded SnS_2 without using Ce dopant can further reduce the lithiation-induced volume expansion. Hence, the modified SnS_2 materials possess better stability than the pristine SnS_2. The theoretical open circuit potential (U) is calculated by using

$$U = \frac{E_{Li_xSnS_2} - E_{SnS_2} - NE_{Li}}{-N \cdot e}$$

Here $E_{Li_xSnS_2}$ E_{SnS_2} are the total energies of lithiated and nonlithiated $3 \times 3 \times 2$ SnS_2 supercell, respectively. E_{Li} is the energy per Li atom in bcc Li crystal. N is the number of Li atoms in SnS_2 matrix, and e is the elementary charge. In our study, the averaged open circuit potential is around 1.2 V for both Li_3SnS_2 and $Li_3Ce_{0.05}Sn_{0.95}S_2$, which perfectly agrees with

DOI: 10.1021/am5068707
ACS Appl. Mater. Interfaces 2015, 7, 4000−4009

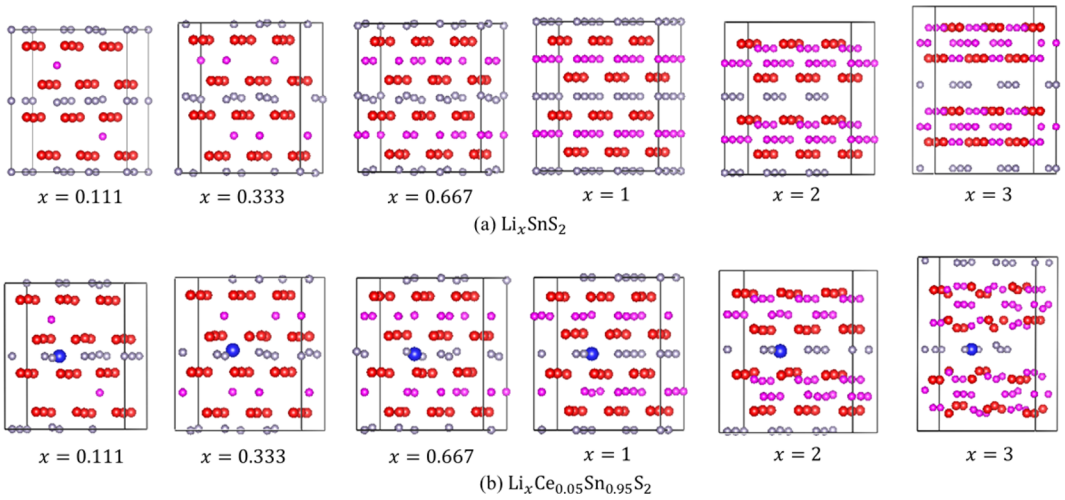

Figure 8. Geometric structures of (a) Li_xSnS_2 and (b) $Li_xCe_{0.05}Sn_{0.95}S_2$. Sn atoms are represented by gray balls, S atoms are represented by red balls, Ce atom is represent by a dark blue ball, and Li atoms are represented by violet balls.

the plateau value of voltage profile measured in the experiment.[69]

The atom structures of Li_xSnS_2 with different lithium content are shown in Figure 8. When the Li content (x) is below 1, foreigner atoms prefer to occupy octahedral sites, and the volume expansion increases slowly as shown in Figure 7. At x = 2, Li atoms occupy both octahedral and tetrahedral sites. At x = 3, tetrahedral Li atoms move into S layer and LiS−Li−LiS trilayer appears between two Sn monolayers. For x = 2, we still considered initial models with Li atoms in the Sn layer. These atoms moved out of Sn layer and finally settled at tetrahedral sites finally as shown in Figure 8. For x = 3, we also considered initial models with Li atom in the Sn layer. Similarly, these Li atoms move into S layers during the structure optimization.

The electronic states variation with lithium content are also investigated. The averaged net charge of each element with different lithiation state is plotted in Figure 9. For nondoped SnS_2, the Sn^{4+} ions cannot be reduced in a low Li content region ($0 < x \leq 1$). In this region, S^{2-} is continuously reduced to $S^{2.5-}$ as Li content rises to 1. After x = 1, Sn cations are significantly reduced by Li intercalation. Meanwhile, S anions lose negative charge when Li content is larger than 1, as shown in Figure 9. For Ce-doped SnS_2, Sn^{4+} ions start to get electrons at x = 0.667, which means that the dopant can assist Li to reduce Sn cations. The Li content slightly affects the electronic state of Ce. As discussed above, Ce is positively charged by 1.86 e at nonlithiated state. As Li content increases to x = 3, Ce cation is monotonically reduced from $Ce^{1.86+}$ to $Ce^{1.63+}$. Figure 10 shows the distribution of electron density on the (110)

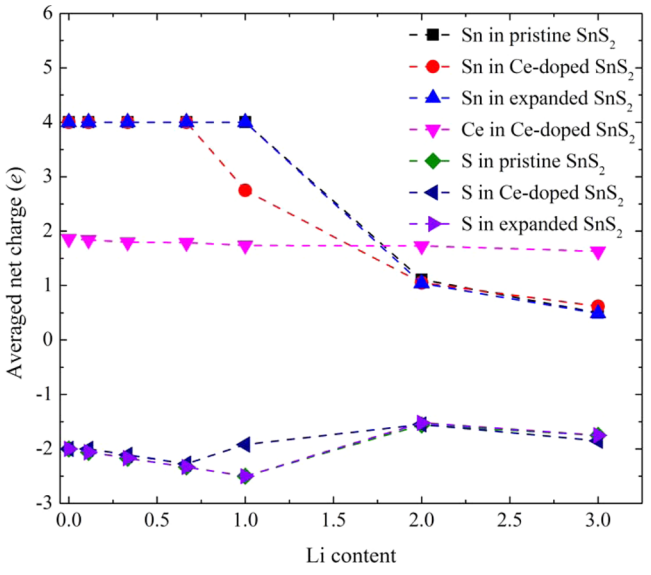

Figure 9. Variation of averaged net charge of each element as Li content increases.

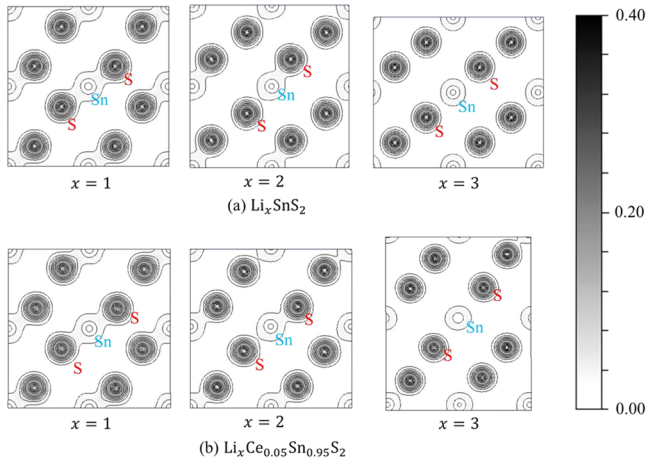

Figure 10. Distribution of electron density (e/Å^3) on the (110) plane of (a) pristine and (b) Ce-doped SnS_2.

plane. It is found that the Sn−S bond is gradually broken by increasing Li content. Figure 10 clearly demonstrates that Sn−S bond disappears at x = 3. The lithiation process is related to Sn reduction and S−Sn−S trilayer decomposition. In this process, LiS−Li−LiS trilayer forms between two Sn monolayers.

As discussed above, the lithiation process of SnS_2-based material can be divided to two stages. When the Li content is smaller than 1 ($x \leq 1$), the intercalated Li atoms occupy octahedral sites and induce a small volume expansion. When the Li content is larger than 1 ($x > 1$), SnS_2 gradually decomposes accompanied by the formation of lithium sulfide and large volume expansion. Although the lithiation process of

DOI: 10.1021/am5068707
ACS Appl. Mater. Interfaces 2015, 7, 4000−4009

SnS_2 is similar to that of molybdenum disulfide (MoS_2), the mechanism of volume expansion for the former one is different from the later one. Stephenson et al. reviewed the lithiation mechanism of MoS_2, and they concluded that the volume expansion is attributed to the Li ionic state.[70] They thought the ionicity of Li decreases as the Li concentration increases to 1. Meantime, the radius of Li increases because Li^+ has a radius around 0.7 Å and neural Li has a radius around 1.4 Å.[71] Hence, the increase of Li radius during the lithiation induces a volume expansion. However, our simulation finds that Li remains fully ionized (Li is positively charged by +1 e) during the SnS_2 lithiation process. Hence the volume expansion induced by lithiation cannot be attributed to the radius variation of Li. The volume expansion of Li_xSnS_2 can be explained by the Coulomb repulsion between two S−Sn−S layers. As shown in Figure 9, S gains negative charge as Li content increases to 1, while the electronic state of Sn remains unchanged. Obviously, S−Sn−S layers are negatively charged, and the Coulomb force between them induces a lattice expansion along the [001] direction. When the Li content is larger than 1, Sn^{4+} is reduced to neutral Sn during the lithiation process, which is accompanied by the increase of Sn radius. In this stage, the volume expansion is attributed to the ionicity of Sn.

CONCLUSIONS

In conclusion, the intercalation and diffusion of Li in SnS_2 interlayer are investigated by the first-principles approach. It is found that the OIS is energetically favored for Li occupation due to its more negative formation energy than the TIS. Volume expansion is observed when a Sn atom is substituted by a Ce atom. The SnS_2 expansion can lower the formation energy because the tetrahedral/octahedral volume is enlarged to accept a foreigner Li atom. The electronic structure analysis proves that interstitial Li can interact with Ce dopant. Interstitial Li atom tends to diffuse from one OIS to the neighbor one via a TIS. The CI-NEB calculations predict that volume expansion is beneficial for lowering the diffusion barrier from the OIS to the TIS. Although Ce dopant is helpful to increase the interlay spacing to reduce the Li diffusion barrier, the attractive interaction between Ce dopant and Li negatively impacts Li diffusivity in SnS_2 interlayer. We suggest development of novel synthesis methods without using dopant to optimize interlayer spacing, such as vertically growing SnS_2 layer on a template with appropriate geometry. The volume expansion induced by Li intercalation is studied in the present study. It is found that the volume expansion with low Li content ($x \leq 1$) is not dramatic. The deeper lithiation ($1 < x \leq 3$) generates steep volume expansion. In this lithiation process, Sn^{4+} cations are significantly reduced, the S−Sn−S trilayer decomposes, and LiS−Li−LiS trilayer forms between Sn monolayers.

AUTHOR INFORMATION

Corresponding Authors

*E-mail: hqdeng@hnu.edu.cn.
*E-mail:pmukherjee@tamu.edu.

Notes

The authors declare no competing financial interest.

ACKNOWLEDGMENTS

Financial support from Texas A&M University faculty research initiation grant is gratefully acknowledged. The authors are thankful for the computational resource partly provided by the National Supercomputer Center in Changsha, China.

REFERENCES

(1) Tarascon, J. M. Key Challenges in Future Li-Battery Research. *Philos. Trans. R. Soc., A* **2010**, *368* (1923), 3227−3241.
(2) Tarascon, J. M.; Armand, M. Issues and Challenges Facing Rechargeable Lithium Batteries. *Nature* **2001**, *414* (6861), 359−367.
(3) Etacheri, V.; Marom, R.; Elazari, R.; Salitra, G.; Aurbach, D. Challenges in the Development of Advanced Li-Ion Batteries: A Review. *Electrochem. Solid-State Lett.* **2011**, *4* (9), 3243−3262.
(4) Armand, M.; Tarascon, J. M. Building Better Batteries. *Nature* **2008**, *451* (7179), 652−657.
(5) Xu, B.; Qian, D.; Wang, Z.; Meng, Y. S. Recent Progress in Cathode Materials Research for Advanced Lithium Ion Batteries. *Mater. Sci. Eng., R.* **2012**, *73* (5), 51−65.
(6) Ammundsen, B.; Paulsen, J. Novel Lithium-Ion Cathode Materials Based on Layered Manganese Oxides. *Adv. Mater.* **2001**, *13* (12−13), 943−956.
(7) Gao, Y. A.; Yakovleva, M. V.; Ebner, W. B. Novel LiNi1−*x*Ti*x*/2Mg*x*/2O_2 Compounds as Cathode Materials for Safer Lithium-Ion Batteries. *Electrochem. Solid-State Lett.* **1998**, *1* (3), 117−119.
(8) Zhang, B.; Han, Y. D.; Zheng, J. C.; Shen, C.; Ming, L.; Zhang, J. F. A Novel Lithium Vanadium Fluorophosphate Nanosheet with Uniform Carbon Coating as a Cathode Material for Lithium-Ion Batteries. *J. Power Sources* **2014**, *264*, 123−127.
(9) Xiang, X. D.; Xing, L. D.; Li, W. S. A Novel Manganese-Based Lithium-Intercalated Cathode Material with High Cyclic Stability for Lithium-Ion Batteries. *Sci. Adv. Mater.* **2014**, *6* (7), 1506−1510.
(10) Li, J.; Daniel, C.; Wood, D. L. Cathode Manufacturing for Lithium-Ion Batteries. *Handbook of Battery Materials*, 2nd ed.: Wiley; New York, 2011; pp 939−960.
(11) Li, J. L.; Armstrong, B. L.; Kiggans, J.; Daniel, C.; Wood, D. L. Optimization of $LiFePO_4$ Nanoparticle Suspensions with Polyethyleneimine for Aqueous Processing. *Langmuir* **2012**, *28* (8), 3783−3790.
(12) Li, J. L.; Armstrong, B. L.; Kiggans, J.; Daniel, C.; Wood, D. L. Lithium Ion Cell Performance Enhancement Using Aqueous $LiFePO_4$ Cathode Dispersions and Polyethyleneimine Dispersant. *J. Electrochem. Soc.* **2013**, *160* (2), A201−A206.
(13) Liu, G.; Zheng, H.; Kim, S.; Deng, Y.; Minor, A. M.; Song, X.; Battaglia, V. S. Effects of Various Conductive Additive and Polymeric Binder Contents on the Performance of a Lithium-Ion Composite Cathode. *J. Electrochem. Soc.* **2008**, *155* (12), A887−A892.
(14) Liu, G.; Zheng, H.; Simens, A. S.; Minor, A. M.; Song, X.; Battaglia, V. S. Optimization of Acetylene Black Conductive Additive and PVDF Composition for High-Power Rechargeable Lithium-Ion Cells. *J. Electrochem. Soc.* **2007**, *154* (12), A1129−A1134.
(15) Liu, G.; Zheng, H.; Song, X.; Battaglia, V. S. Particles and Polymer Binder Interaction: A Controlling Factor in Lithium-Ion Electrode Performance. *J. Electrochem. Soc.* **2012**, *159* (3), A214−A221.
(16) Zheng, H. H.; Yang, R. Z.; Liu, G.; Song, X. Y.; Battaglia, V. S. Cooperation between Active Material, Polymeric Binder, and Conductive Carbon Additive in Lithium Ion Battery Cathode. *J. Phys. Chem. C* **2012**, *116* (7), 4875−4882.
(17) Wang, Y.; Lee, J. Y. Molten Salt Synthesis of Tin Oxide Nanorods: Morphological and Electrochemical Features. *J. Phys. Chem. B* **2004**, *108* (46), 17832−17837.
(18) Yan, D.; Bai, Y.; Yu, C. Y.; Li, X. G.; Zhang, W. F. A Novel Pineapple-Structured Si/TiO_2 Composite as Anode Material for Lithium Ion Batteries. *J. Alloys Compd.* **2014**, *609*, 86−92.
(19) Chen, N.; Yao, Y.; Wang, D.; Wei, Y.; Bie, X.; Wang, C.; Chen, G.; Du, F. $LiFe(MoO_4)_2$ as a Novel Anode Material for Lithium-Ion Batteries. *ACS Appl. Mater. Interfaces.* **2014**, *6* (13), 10661−6.
(20) Feng, J. K.; Xiong, S. L.; Qian, Y. T.; Yin, L. W. Synthesis of Nanosized Cadmium Oxide (CdO) as a Novel High Capacity Anode Material for Lithium-Ion Batteries: Influence of Carbon Nanotubes Decoration and Binder Choice. *Electrochim. Acta* **2014**, *129*, 107−112.

DOI: 10.1021/am5068707
ACS Appl. Mater. Interfaces 2015, 7, 4000−4009

(21) Courtney, I. A.; Dahn, J. Key Factors Controlling the Reversibility of the Reaction of Lithium with SnO_2 and Sn_2 BPO 6 Glass. *J. Electrochem. Soc.* **1997**, *144* (9), 2943−2948.
(22) Zhou, X.; Zou, Y.; Yang, J. Periodic Structures of Sn Self-Inserted between Graphene Interlayers as Anodes for Li-Ion Battery. *J. Power Sources* **2014**, *253*, 287−293.
(23) Xu, Y.; Liu, Q.; Zhu, Y.; Liu, Y.; Langrock, A.; Zachariah, M. R.; Wang, C. Uniform Nano-Sn/C Composite Anodes for Lithium Ion Batteries. *Nano Lett.* **2013**, *13* (2), 470−474.
(24) Qin, J.; He, C.; Zhao, N.; Wang, Z.; Shi, C.; Liu, E.-Z.; Li, J. Graphene Networks Anchored with Sn@Graphene as Lithium Ion Battery Anode. *ACS Nano* **2014**, *8* (2), 1728−1738.
(25) Pol, V. G.; Wen, J.; Miller, D. J.; Thackeray, M. M. Sonochemical Deposition of Sn, SnO_2, and Sb on Spherical Hard Carbon Electrodes for Li-Ion Batteries. *J. Electrochem. Soc.* **2014**, *161* (5), A777−A782.
(26) Zhou, H.; Zhou, W.-p.; Adzic, R. R.; Wong, S. S. Enhanced Electrocatalytic Performance of One-Dimensional Metal Nanowires and Arrays Generated via an Ambient, Surfactantless Synthesis. *J. Phys. Chem. C* **2009**, *113* (14), 5460−5466.
(27) Alia, S. M.; Larsen, B. A.; Pylypenko, S.; Cullen, D. A.; Diercks, D. R.; Neyerlin, K. C.; Kocha, S. S.; Pivovar, B. S. Platinum-Coated Nickel Nanowires as Oxygen-Reducing Electrocatalysts. *ACS Catal.* **2014**, *4* (4), 1114−1119.
(28) Cherepy, N. J.; Liston, D. B.; Lovejoy, J. A.; Deng, H.; Zhang, J. Z. Ultrafast Studies of Photoexcited Electron Dynamics in γ-and α-Fe_2O_3 Semiconductor Nanoparticles. *J. Phys. Chem. B* **1998**, *102* (5), 770−776.
(29) Rowsell, J. L. C.; Pralong, V.; Nazar, L. F. Layered Lithium Iron Nitride: A Promising Anode Material for Li-Ion Batteries. *J. Am. Chem. Soc.* **2001**, *123* (35), 8598−8599.
(30) Wang, Z.; Su, Q.; Deng, H. Single-Layered V_2O_5, a Promising Cathode Material for Rechargeable Li and Mg Ion Batteries: An Ab Initio Study. *Phys. Chem. Chem. Phys.* **2013**, *15* (22), 8705−8709.
(31) Lefebvre-Devos, I.; Olivier-Fourcade, J.; Jumas, J.; Lavela, P. Lithium Insertion Mechanism in SnS_2. *Phys. Rev. B* **2000**, *61* (4), 3110.
(32) Kim, T. J.; Kirn, C.; Son, D.; Choi, M.; Park, B. Novel SnS_2-Nanosheet Anodes for Lithium-Ion Batteries. *J. Power Sources* **2007**, *167* (2), 529−535.
(33) Wang, L. Y.; Zhuo, L. H.; Yu, Y. C.; Zhao, F. Y. High-Rate Performance of SnS_2 Nanoplates without Carbon-Coating as Anode Material for Lithium Ion Batteries. *Electrochim. Acta* **2013**, *112*, 439−447.
(34) Zhai, C. X.; Du, N.; Zhang, H.; Yu, J. X.; Yang, D. R. Multiwalled Carbon Nanotubes Anchored with SnS_2 Nanosheets as High-Performance Anode Materials of Lithium-Ion Batteries. *ACS Appl. Mater. Interfaces* **2011**, *3* (10), 4067−4074.
(35) Liu, S. Y.; Lu, X.; Xie, J.; Cao, G. S.; Zhu, T. J.; Zhao, X. B. Preferential *c*-Axis Orientation of Ultrathin SnS_2 Nanoplates on Graphene as High-Performance Anode for Li-Ion Batteries. *ACS Appl. Mater. Interfaces* **2013**, *5* (5), 1588−1595.
(36) Xie, X. Q.; Su, D. W.; Chen, S. Q.; Zhang, J. Q.; Dou, S. X.; Wang, G. X. SnS_2 Nanoplatelet@Graphene Nanocomposites as High-Capacity Anode Materials for Sodium-Ion Batteries. *Chem—Asian J.* **2014**, *9* (6), 1611−1617.
(37) Zhong, H.; Yang, G.; Song, H.; Liao, Q.; Cui, H.; Shen, P.; Wang, C.-X. Vertically Aligned Graphene-like SnS_2 Ultrathin Nanosheet Arrays: Excellent Energy Storage, Catalysis, Photoconduction, and Field-Emitting Performances. *J. Phys. Chem. C* **2012**, *116* (16), 9319−9326.
(38) Wang, Q. F.; Huang, Y.; Miao, J.; Zhao, Y.; Wang, Y. Synthesis and Electrochemical Characterizations of Ce Doped SnS_2 Anode Materials for Rechargeable Lithium Ion Batteries. *Electrochim. Acta* **2013**, *93*, 120−130.
(39) Wang, Q.; Huang, Y.; Miao, J.; Zhao, Y.; Zhang, W.; Wang, Y. Graphene-Supported Ce−SnS_2 Nanocomposite as Anode Material for Lithium-Ion Batteries. *J. Am. Ceram. Soc.* **2013**, *96* (7), 2190−2196.
(40) Deng, C.; Zhang, S.; Yang, S. Y.; Gao, Y.; Wu, B.; Ma, L.; Fu, B. L.; Wu, Q.; Liu, F. L. Effects of Ti and Mg Codoping on the Electrochemical Performance of $Li_3V_2(PO_4)_3$ Cathode Material for Lithium Ion Batteries. *J. Phys. Chem. C* **2011**, *115* (30), 15048−15056.
(41) Ceder, G.; Chiang, Y. M.; Sadoway, D. R.; Aydinol, M. K.; Jang, Y. I.; Huang, B. Identification of Cathode Materials for Lithium Batteries Guided by First-Principles Calculations. *Nature* **1998**, *392* (6677), 694−696.
(42) Meng, Y. S.; Arroyo-de Dompablo, M. E. First Principles Computational Materials Design for Energy Storage Materials in Lithium Ion Batteries. *Energ Environ. Sci.* **2009**, *2* (6), 589−609.
(43) Ceder, G. Opportunities and Challenges for First-Principles Materials Design and Applications to Li Battery Materials. *MRS Bull.* **2010**, *35* (09), 693−701.
(44) Kresse, G.; Hafner, J. Ab Initio Molecular Dynamics for Open-Shell Transition Metals. *Phys. Rev. B* **1993**, *48* (17), 13115.
(45) Kresse, G.; Furthmüller, J. Efficient Iterative Schemes for Ab Initio Total-Energy Calculations Using a Plane-Wave Basis Set. *Phys. Rev. B* **1996**, *54* (16), 11169.
(46) Kohn, W.; Sham, L. J. Self-Consistent Equations Including Exchange and Correlation Effects. *Phys. Rev.* **1965**, *140* (4A), A1133.
(47) Kresse, G.; Joubert, D. From Ultrasoft Pseudopotentials to the Projector Augmented-Wave Method. *Phys. Rev. B* **1999**, *59* (3), 1758.
(48) Perdew, J. P.; Burke, K.; Ernzerhof, M. Generalized Gradient Approximation Made Simple. *Phys. Rev. Lett.* **1996**, *77* (18), 3865−3868.
(49) Monkhorst, H. J.; Pack, J. D. Special Points for Brillouin-Zone Integrations. *Phys. Rev. B* **1976**, *13* (12), 5188.
(50) Henkelman, G.; Uberuaga, B. P.; Jónsson, H.; Climbing Image, A. Nudged Elastic Band Method for Finding Saddle Points and Minimum Energy Paths. *J. Chem. Phys.* **2000**, *113* (22), 9901−9904.
(51) Hazen, R. M.; Finger, L. W. Crystal-Structures and Compressibilities of Layer Minerals at High-Pressure. 1. SnS_2, Berndtite. *Am. Mineral.* **1978**, *63* (3−4), 289−292.
(52) Wahnón, P.; Conesa, J. C.; Palacios, P.; Lucena, R.; Aguilera, I.; Seminovski, Y.; Fresno, F. V-Doped SnS_2: A New Intermediate Band Material for a Better Use of the Solar Spectrum. *Phys. Chem. Chem. Phys.* **2011**, *13* (45), 20401−20407.
(53) Burton, L. A.; Walsh, A. Phase Stability of the Earth-Abundant Tin Sulfides SnS, SnS_2, and Sn_2S_3. *J. Phys. Chem. C* **2012**, *116* (45), 24262−24267.
(54) Henkelman, G.; Arnaldsson, A.; Jónsson, H. A Fast and Robust Algorithm for Bader Decomposition of Charge Density. *Comput. Mater. Sci.* **2006**, *36* (3), 354−360.
(55) Sanville, E.; Kenny, S. D.; Smith, R.; Henkelman, G. Improved Grid-Based Algorithm for Bader Charge Allocation. *J. Comput. Chem.* **2007**, *28* (5), 899−908.
(56) Tang, W.; Sanville, E.; Henkelman, G.; Grid-Based Bader, A. Analysis Algorithm without Lattice Bias. *J. Phys.: Condens. Matter.* **2009**, *21* (8), 084204.
(57) Wang, Z.; Su, Q.; Deng, H.; He, W.; Lin, J.; Fu, Y. Modelling and Simulation of Electron-Rich Effect on Li Diffusion in Group IVA Elements (Si, Ge, and Sn) for Li Ion Batteries. *J. Mater. Chem. A* **2014**, *2* (34), 13976−13982.
(58) Arrouvel, C.; Parker, S. C.; Islam, M. S. Lithium Insertion and Transport in the TiO_2−B Anode Material: A Computational Study. *Chem. Mater.* **2009**, *21* (20), 4778−4783.
(59) Fan, X. F.; Zheng, W. T.; Kuo, J. L. Adsorption and Diffusion of Li on Pristine and Defective Graphene. *ACS Appl. Mater. Interfaces.* **2012**, *4* (5), 2432−2438.
(60) Tritsaris, G. A.; Kaxiras, E.; Meng, S.; Wang, E. G. Adsorption and Diffusion of Lithium on Layered Silicon for Li-Ion Storage. *Nano Lett.* **2013**, *13* (5), 2258−2263.
(61) Li, Y. F.; Wu, D. H.; Zhou, Z.; Cabrera, C. R.; Chen, Z. F. Enhanced Li Adsorption and Diffusion on MoS_2 Zigzag Nanoribbons by Edge Effects: A Computational Study. *J. Phys. Chem. Lett.* **2012**, *3* (16), 2221−2227.
(62) Morgan, D.; Van der Ven, A.; Ceder, G. Li Conductivity in Li_xMPO_4 (M = Mn, Fe, Co, Ni) Olivine Materials. *Electrochem. Solid-State Lett.* **2004**, *7* (2), A30−A32.

DOI: 10.1021/am5068707
ACS Appl. Mater. Interfaces 2015, 7, 4000−4009

(63) Wang, Z.; Su, Q.; Shi, J.; Deng, H.; Yin, G. Q.; Guan, J.; Wu, M. P.; Zhou, Y. L.; Lou, H. L.; Fu, Y. Q. Comparison of Tetragonal and Cubic Tin as Anode for Mg Ion Batteries. *ACS Appl. Mater. Interfaces.* **2014**, *6* (9), 6786−6789.
(64) Wu, J.; Gao, G.; Wu, G.; Liu, B.; Yang, H.; Zhou, X.; Wang, J. Tavorite-$FeSO_4F$ as a Potential Cathode Material for Mg Ion Batteries: A First Principles Calculation. *Phys. Chem. Chem. Phys.* **2014**, *16*, 22974−22978.
(65) Ding, L. P.; He, S. L.; Miao, S. D.; Jorgensen, M. R.; Leubner, S.; Yan, C. L.; Hickey, S. G.; Eychmuller, A.; Xu, J. Z.; Schmidt, O. G. Ultrasmall SnO_2 Nanocrystals: Hot-Bubbling Synthesis, Encapsulation in Carbon Layers and Applications in High Capacity Li-Ion Storage. *Sci. Rep.* **2014**, *4*, 4676.
(66) Huggins, R. A. Lithium Alloy Negative Electrodes. *J. Power Sources* **1999**, *81*−*82* (0), 13−19.
(67) Beaulieu, L.; Eberman, K.; Turner, R.; Krause, L.; Dahn, J. Colossal Reversible Volume Changes in Lithium Alloys. *Electrochem. Solid-State Lett.* **2001**, *4* (9), A137−A140.
(68) Enyashin, A. N.; Seifert, G. Density-Functional Study of Li_xMoS_2 Intercalates ($0 \leq x \leq 1$). *Comput. Theor. Chem.* **2012**, *999*, 13−20.
(69) Seo, J. W.; Jang, J. T.; Park, S. W.; Kim, C. J.; Park, B. W.; Cheon, J. W. Two-Dimensional SnS_2 Nanoplates with Extraordinary High Discharge Capacity for Lithium Ion Batteries. *Adv. Mater.* **2008**, *20* (22), 4269−4273.
(70) Stephenson, T.; Li, Z.; Olsen, B.; Mitlin, D. Lithium Ion Battery Applications of Molybdenum Disulfide (MoS_2) Nanocomposites. *Energ Environ. Sci.* **2014**, *7* (1), 209−231.
(71) Silbernagel, B.; Whittingham, M. An NMR Study of the Alkali Metal Intercalation Phase Li_xTiS_2: Relation to Structure, Thermodynamics, and Ionicity. *J. Chem. Phys.* **1976**, *64* (9), 3670−3673.

DOI: 10.1021/am5068707
ACS Appl. Mater. Interfaces 2015, 7, 4000−4009